Vietnam Journal of Mechanics, Vol. 47, No. 2 (2025), pp. 259 – 274
DOI: https://doi.org/10.15625/0866-7136/22383

NUMERICAL INVESTIGATION OF ELECTRO-CONJUGATE FLUID MICRO-PUMP UNDER THE EFFECTS OF DOWNSTREAM ANGLE AND THE NEGATIVE ELECTRODE WIDTH

Van Tran Do[1,2], The Khanh Lai[1], Toan Thang Vu[1], Thi Anh Nguyen[3], Ich Long Ngo[1,*]
[1] *School of Mechanical Engineering, Hanoi University of Science and Technology, No. 1 Dai Co Viet, Hanoi, Vietnam*
[2] *Faculty of Mechanical Engineering, University of Transport and Communications, No. 3 Cau Giay, Hanoi, Vietnam*
[3] *School of Electrical and Electronic Engineering, Hanoi University of Science and Technology, No. 1 Dai Co Viet, Hanoi, Vietnam*
[*] E-mail: long.ngoich@hust.edu.vn

Received: 06 February 2025 / Revised: 27 May 2025 / Accepted: 10 June 2025
Published online: 09 August 2025

Abstract. This paper describes a numerical study of the electro-hydrodynamic behaviors of the fluid flow in an electro-conjugate fluid (ECF) micro-pump under the effects of the collector electrode width (L_c) and its downstream angle (α_2). The finite element method was used to examine the characteristics of the ECF micro-pump with the applied voltage ranging from 2 kV to 8 kV, L_c ranging from 0.0 to 4.0, and α_2 ranging from 30° to 90°. Consequently, the numerical results indicated that the ECF flow characteristics and the operating ranges of this ECF micro-pump are affected significantly by α_2 and L_c of the negative electrode. Indeed, the operating range of the ECF micro-pump can be further extended by reducing α_2, particularly at higher flow rates. Moreover, the operating ranges of both pressure difference (Δp) and flow rate of the ECF micro-pump can be extended when L_c varies in the optimum range, i.e., from 0.5 to 2.0. The maximum efficiency of such an ECF micro-pump was 7.4% at $\phi_0 = 8$ kV and $L_c = 2.0$. These results play a critical role in understanding the electro-hydrodynamic behaviors of the fluid flow in an ECF micro-pump, and they can be applied in mechanical and biomedical engineering fields.

Keywords: electro-conjugate fluid, finite element method, micro-pump.

1. INTRODUCTION

Nowadays, the development of science and technology has contributed to the rapid progress of microfluidic devices with many applications [1]. Micro-pumps are widely applied to microfluidic devices. Based on the principle of creating fluid flow movement, micro-pumps are divided into mechanical micro-pumps (with moving parts) and non-mechanical micro-pumps (without moving parts). ECF (Electro-Conjugate Fluid) micro-pumps are attracting much attention [2–4]. ECF is a type of functional fluid in which a strong flow is generated between the gap of a pair of electrodes when a high DC voltage is applied to the electrodes [5]. This strong flow is referred to as the electro-conjugate effect (ECF jet flow), and the ECF flow is dominated by the Coulomb, dielectric, and electrostriction forces [6]. ECF micro-pumps can operate with low vibration, smoothness, low noise, and high power density because electrical energy is converted directly into kinetic energy of ECF flow [7, 8]. Furthermore, the structure of ECF micro-pumps is simple, without moving components and has low friction. ECF micro-pumps are widely used in soft robots [9, 10], cooling electronic microchips [11–13], and creating new drugs [14].

Although ECF micro-pumps have many advantages and potential applications in various fields, they often have very low efficiencies of only a few percent [10]. Their performance depends on the electrode configuration [12, 15]. Many studies have focused on changing the electrode shape design to obtain the highest performance in ECF micro-pumps. Initially, to study the ECF flow behavior in micro-pumps, three different types of electrode pairs were proposed: thin planar electrode pairs [13], triangular prism electrode pairs [16], and ring electrode pairs [17]. Research shows that the triangular prism electrode pairs have outstanding advantages over the other types due to their high power density and easy integration of MEMS technology in fabrication. Recently, studies have proposed rectangular electrode configurations to investigate the effect of this electrode configuration on the flow in ECF micro-pumps. The study showed that adjusting the electrode configuration can control the flow [15]. The arrangement of parallel or series electrode configurations has also been considered to affect the pressure and flow of the micro-pump [12]. The research group of Han evaluated the effect of triangular prism electrodes and slit electrodes on the performance of ECF micro-pumps. The study focused on the consideration of the slit electrode width, the tip angle of a triangular prism electrode, and the gap between the triangular prism electrode and slit one on the performance of ECF micro-pumps [18]. Most recently, our research team focused on evaluating the influence of the emitter angle and collector angle on the flow behavior in ECF micro-pumps [19]. However, no study has examined the influence of the downstream angle and the collector electrode width on the fluid flow behavior in ECF micro-pumps.

This paper investigates some electrohydrodynamic behaviors of fluid flow in electro-conjugate fluid micro-pumps under the influence of the collector electrode width (L_c) and its shape, which is adjusted by the downstream angle (α_2). This problem is solved by numerical simulation using the finite element method. Section 2 shows the numerical method with the appropriate code validation. The numerical results are summarized, analyzed, and discussed in Section 3. Section 3.1 focuses on considering the impact of the downstream angle on the velocity, concentration, and micro-pump characteristic curves. Section 3.2 examines the effects of the collector's width. Finally, the conclusions obtained from this study are shown in Section 4.

2. METHODOLOGY

2.1. Mathematical model

Fig. 1 illustrates the schematic principle of the ECF micro-pumps with some basic dimensions: L_c and H_c are the lengths of the slit electrode, α_2 is the downstream angle, D_t is the distance between the collector electrode and the emitter electrode, α_1 is the emitter electrode angle, and L_e and H_e are the length and width of the emitter electrode. The upstream and downstream lengths are $12H_c$ and $25H_c$, respectively. These lengths guarantee that the inlet and outlet boundary conditions minimally impact the flow profile. Additionally, the width of the main channels (H) was kept constant at $5H_c$. A teardrop-shaped positive electrode with a length of L_e and an emitter tip angle of α_1 has a thickness of $H_e \sim L_e \tan(\alpha_1/2)/(0.5 + 0.5\tan(\alpha_1/2))$. The downstream angle α_2 is less than or equal to 90°. Moreover, the collector slit has dimensions of L_c and H_c and it is placed at a distance of $D_t = H_c$ from the emitter tip. In the present study, the behaviors of ECF jets in the micro-pump are examined under the effects of the applied voltage on the electrodes, α_2, and L_c.

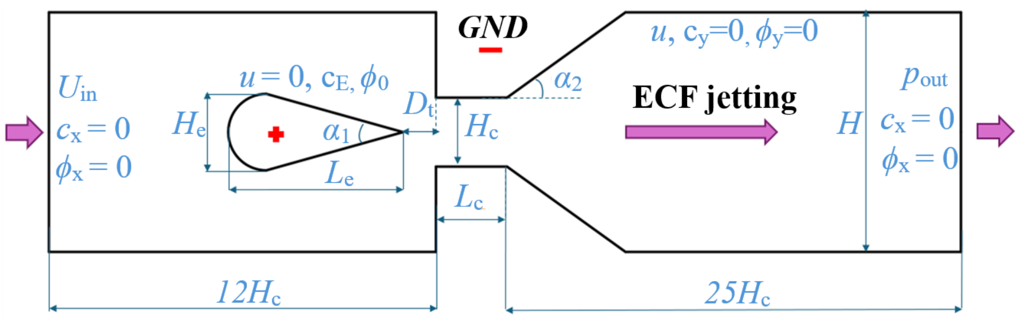

Fig. 1. Schematic of the numerical model and boundary conditions

Establishing continuity, momentum, electrostatics, and species transport equations is necessary to simulate the generated ECF jets. These governing equations are formulated in non-dimensional forms using dimensionless variables shown in Eq. (1).

$$x = \frac{x^*}{H_c}, \quad y = \frac{y^*}{H_c}, \quad u = \frac{u^*}{U_{in}}, \quad p = \frac{p^*}{\rho U_{in}^2}, \quad c = \frac{c^*}{c_0}, \quad \phi = \frac{\phi^*}{\phi_0}, \tag{1}$$

where p^* is the local pressure; $\mathbf{u}^*$ is the local velocity of fluid flow; ϕ^* is the electric potential; H_c is the characteristic length; ϕ_0 is the characteristic applied voltage that is defined as V_e^* applied at the emitter, as shown in Fig. 1; U_{in} is the characteristic velocity at the inlet; and c_0 is the bulk concentration of charges, i.e., $c_0 = k_P^* E_{\text{thresP}}^* / F$, where k_P^* is a proportionality constant characterizing the densities of positive ions; E_{thresP}^* is the threshold field strengths for the positive electrode; and F is Faraday's constant. As a result, the governing equations in their non-dimensional forms are presented in Eqs. (2)–(5).

Continuity: $$\nabla \cdot \mathbf{u} = 0. \tag{2}$$

Momentum: $$(\mathbf{u} \cdot \nabla \mathbf{u}) = \nabla \cdot \left\{ -p\mathbf{I} + \frac{1}{\text{Re}_f} \left[\nabla \mathbf{u} + (\nabla \mathbf{u})^T \right] \right\} + Mc\rho_v \mathbf{E}. \tag{3}$$

Electrostatics: $$-\nabla \cdot \left(\frac{1}{\text{De}^2} \nabla \phi \right) = \rho_v. \tag{4}$$

Species transport: $$\nabla \cdot \left\{ -\frac{1}{\text{Pe}} \nabla c_i - \frac{\phi_C}{\text{Pe}} z_i c_i \nabla \phi + \mathbf{u} c_i - \frac{1}{\text{Re}_E \text{De}^2} \nabla \phi \right\} = 0. \tag{5}$$

The Coulomb, dielectric, and electrostriction forces governed the ECF jet, which was described by the Korteweg–Helmholtz model [20,21]. However, ECF is a pure dielectric, and the fluid flow is incompressible, so the dielectric and electrostriction forces can be neglected for the ECF jet flow in the present study. Therefore, only the Coulomb force drives an ECF flow when a high DC voltage is applied, and this force is the last term on the right-hand side of Eq. (3). The electric field strength is generated by the DC voltage, $\mathbf{E} = -\nabla \phi$, and the space charge density is $\rho_v = \sum z_i c_i$, where z_i and c_i are the charge number and concentration, respectively. Consequently, important parameters are formed in the governing equations, including Re_f (fluid Reynolds number), Re_e (electric Reynolds number), Mc (mobility ratio), and Pe (the Péclet number). These parameters are shown in Eq. (6).

$$\begin{gathered} \text{Re}_f = \frac{\rho U_{in} H_c}{\mu}, \quad \text{Re}_e = \frac{\varepsilon U_{in}}{\sigma H_c}, \quad Mc = \frac{F c_0 \phi_0}{\rho U_{in}^2}, \quad \text{Pe} = \frac{U_{in} H_c}{D_i}, \\ \lambda_D^2 = \frac{\varepsilon \phi_0}{F c_0}, \quad \text{De} = \frac{H_c}{\lambda_D}, \quad \varepsilon = \varepsilon_0 \varepsilon_r, \quad \phi_c = \frac{F \phi_0}{R T_m}. \end{gathered} \tag{6}$$

In Eq. (6), ρ is the fluid density, and μ is the dynamic viscosity. Additionally, De and λ_D are the Debye number and Debye length, respectively; D_i is the diffusion coefficient; ε_0 is the permittivity constant; ε_r is the relative permittivity; R is the gas constant; and T_m is the average temperature under test conditions.

The boundary condition for charge concentration is specified at the surfaces of the emitter and collector, as shown in Eqs. (7)–(9).

$$c_E = \lambda Nu_E \left(E_S - E_{\text{thresP}}\right) \operatorname{sign}\left(\phi_0\right), \tag{7}$$

$$c_N = \kappa Nu_E \left(E_S - E_{\text{thresN}}\right) \operatorname{sign}\left(\phi_0\right), \tag{8}$$

$$Nu_E = \frac{k_P^* \phi_0}{F c_0 H_c}, \quad \kappa = \frac{k_N}{k_P}, \tag{9}$$

where E_s is the electrostatic field strength; E_{thresN} is the threshold field strength for the negative electrode; λ is a correction factor to account for the effects of measurement errors and discrepancies between simulation and experimental results; and k_N is a proportionality constant characterizing the densities of negative ions. The dimensional parameters used as the reference data for computations are also provided in Table 1.

Table 1. A list of dimensional parameters

Parameter	Value	Unit	Parameter	Value	Unit
F	9.65×10^4	C/mol	k_p^*	2.4×10^5	V/m
ε_0	8.85×10^{-12}	F/m	R	8.314	J/(mol.K)
ε_r	4.7	–	T_m	293	K
c_0	1.77×10^{-8}	mol/m^3	D_i	2.74×10^{-8}	m^2/s
ρ	1690	kg/m^3	α_1	30	deg
μ	8.67×10^{-3}	Pa.s	D_t	200	µm
σ	3.3×10^{-9}	S/m	H_c	200	µm

The boundary conditions (BCs) at the inlet include the inlet velocity U_{in}, charge concentration $c_{x=0}$, and inlet potential $\phi_{x=0}$. The outlet boundary conditions include the outlet pressure p_{out}, $c_{x=0}$, and $\phi_{x=0}$. A no-slip BC was used for all channel walls; $c_{y=0}$ and $\phi_{y=0}$ were applied at the walls for species and electric fields, respectively. The charge concentration c_E and potential ϕ_0 were applied at the emitter electrode; otherwise, these parameters were set to zero at the collector electrode.

The initial conditions used in the laminar flow problem are defined as follows: Only the velocity component in the x-direction was set to U_{in}. Otherwise, it was specified as zero. For the electrostatics problem, the initial conditions were set as follows: the initial electric potential ϕ_0 was zero everywhere, and the potential at the positive electrode ϕ was ϕ_0. For the transport of diluted species problem, an initial concentration of c was set to zero everywhere.

The solver settings were configured to sequentially solve the multiphysical problems (laminar, transport of diluted species, and electrostatics) under steady-state conditions.

The solving strategy was implemented by the following three steps: (i) solving the laminar flow and electrostatics problems; (ii) solving the laminar flow and transport of diluted species; (iii) solving all three physical problems simultaneously.

2.2. Code validation

The mathematical model in Section 2.1 is validated by comparing our numerical simulation results with experimental data obtained by Tran et al. [22]. The results are shown in Fig. 2. It was found that a slight difference is observed in the vortex center and vortex intensity, mainly due to numerical errors; however, both results generally resemble each other. Fig. 2(c) illustrates velocity variation, showing that our simulation has a slight deviation compared to the previous simulation from Tran's study. The maximum deviation obtained is less than 9%.

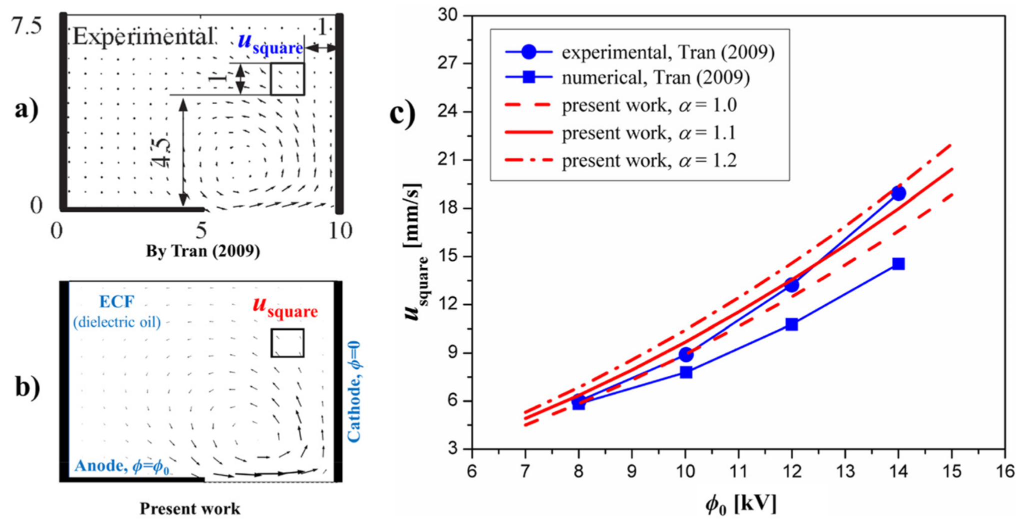

Fig. 2. Model evaluation results compared with experimental results by Tran et al. [22], (a) and (b) velocity vector field, $\phi_0 = -10$ kV, and (c) average velocity in the square according to the applied voltage, with $s = 5$ mm and $T_m = 313$ K [19]

Additionally, the model's reliability was consolidated by comparing the results with those obtained by Nishikawara et al. [23], as shown in Fig. 3. The results indicated that both match well, with a maximum deviation of less than 5%. In summary, this mathematical model was well validated and can be applied for further computations in the present study.

The grid convergence was checked by calculating the pressure difference between the outlet and inlet of the ECF micro-pump ($\Delta p = p_{out} - p_{in}$), where p_{out} and p_{in} are the outlet and inlet pressures, respectively. Eight mesh models (from #1 to #8) were considered, with the number of elements ranging from 1900 to 24880. COMSOL Multiphysics'

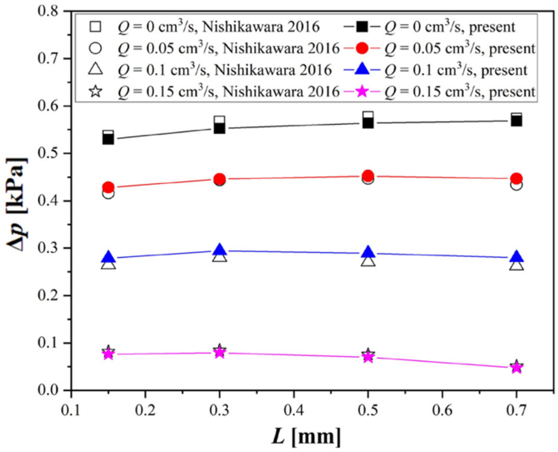

Fig. 3. Pressure difference Δp as a function of the electrode length for $\phi_0 = 5$ kV [19]

adaptive mesh refinement algorithm was used for each mesh model. The next finer mesh was used to compare the relative error of each model in the pressure difference (ε_t). As a result, ε_t gradually decreases and converges with mesh model #7, which has an error of only 0.23% compared to the next finer mesh, as shown in Fig. 4. Therefore, model #7 was used as the base mesh model for the whole computation.

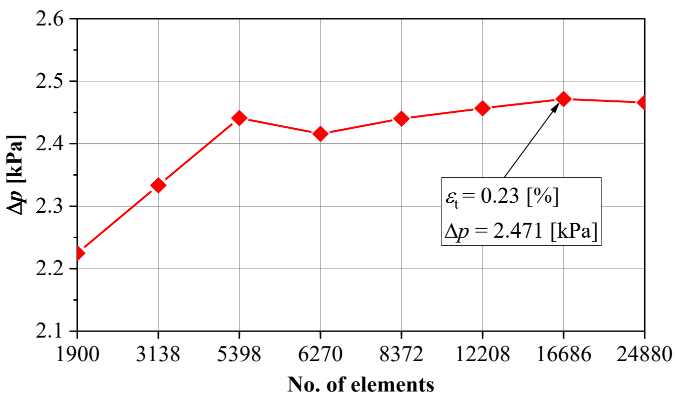

Fig. 4. Grid convergence test ($\mathrm{Re}_f = 1.08$, $\phi_0 = 4$ kV, $L_c = 0.5$ and $\alpha_2 = 30°$)

3. RESULTS AND DISCUSSIONS

3.1. Effects of the downstream angle

Fig. 5 shows the qualitative results of the velocity field and charge concentration distributions for various values of α_2 at the same flow rate of $Q = 50$ ml/h and $\phi_0 = 4$ kV.

The results from Fig. 5(a) indicate that a strong ECF jet is generated through the gap of the collector electrode. Specifically, the maximum velocity field is concentrated mainly at the gap between the two electrodes, implying that a strong fluid flow passes through this gap. When α_2 varies from 90° to 30°, the distribution of the velocity field changes slightly, and the maximum velocity tends to increase gradually. ECF flow is generated by the electric field force acting on the ions in the fluid, and the ECF flow rate highly depends on the charge concentration, which is clearly shown in Fig. 5(b). Specifically, the region in the gap between the two electrodes with the highest velocity field also has the highest charge concentration. Furthermore, as the angle α_2 is decreased from 90° to 30°, the maximum charge concentration tends to increase gradually. This demonstrates that a higher charge concentration increases the flow velocity. These results also predict the changes in the dynamic behaviors of the fluid flow in the ECF micro-pump under the downstream angle effects of the collector electrode.

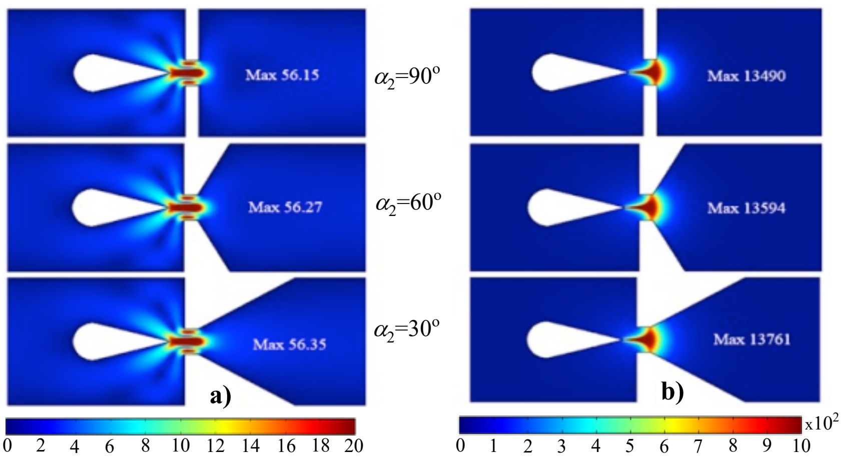

Fig. 5. Distribution of (a) velocity and (b) concentration for various values of α_2 with $Q = 50$ ml/h, $L_c = 0.5$ and $\phi_0 = 4$ kV

Fig. 6 shows the calculation results of the streamline distribution for various downstream angles (α_2) at two specific values of the flow rate, $Q = 50$ ml/h (Fig. 6(a)) and $Q = 200$ ml/h (Fig. 6(b)). The streamline distribution changes slightly at a low flow rate when α_2 decreases from 90° to 30°, as shown in Fig. 6(a). However, the streamline is greatly affected by α_2 at higher flow rates, as indicated in Fig. 6(b). For more detail, when the α_2 decreases, the vortex formation in the ECF micro-pumps gradually decreases, and the vortex area becomes smallest at $\alpha_2 = 30°$. This result implies that the hydraulic losses in such an ECF micro-pump can be reduced when α_2 decreases. Therefore, pump efficiency and outlet flow rate are predicted to improve when the downstream angle of the collector electrode decreases. The influence of the angle (α_2) on the performance of the

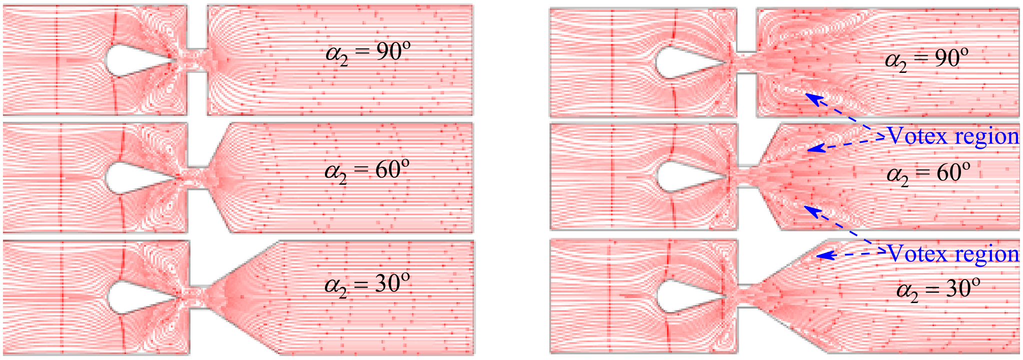

(a) $Q = 50$ ml/h (b) $Q = 200$ ml/h

Fig. 6. Streamline distribution for various values of α_2, (a) $Q = 50$ ml/h, and (b) $Q = 200$ ml/h. $L_c = 1.0$ and $\phi_0 = 4$ kV were used for both cases

ECF micro-pump can be explained as follows: For a smaller α_2, the cross-sectional area at the channel downstream decreases, the flow can move along the channel surfaces, leading to an increase in hydrodynamic characteristics and a reduction in vortex formation, as clearly shown in Fig. 6. This results in decreased energy losses or flow resistance, and hence, the pump efficiency generally increases compared to the case of a large α_2.

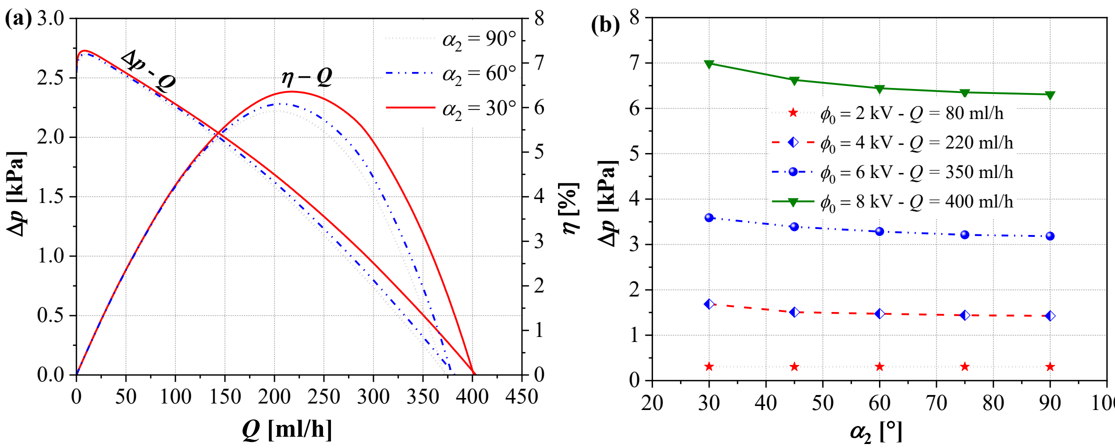

Fig. 7. (a) Characteristic curves for various values of α_2 with $\phi_0 = 4$ kV and (b) Δp–α_2 curves for various values of ϕ_0 with $Q = 120$ ml/h. $L_c = 1.0$ was used for all cases

Fig. 7(a) shows the results of calculating the pump characteristic curves Δp–Q and η–Q with various values of α_2. The efficiency of the ECF micro-pump is determined by Eq. (10), where N_p represents the hydraulic power ($N_p = \Delta p \times Q$) and N_e denotes the electrical power ($N_e = \phi_0 \times I$, where I is the electric current measured at the electrodes).

$$\eta = \frac{N_p}{N_e}. \tag{10}$$

Generally, these characteristic curves are similar to the distinctive curves of turbo-pumps with moving blades, but with a lower value range. When the angle α_2 decreases from 90° to 30°, the characteristic curves Δp–Q and η–Q tend to lift, as shown in Fig. 7(a) (from the black dashed line to the red solid line). This figure also indicates that the maximum efficiency increases by decreasing α_2. Indeed, the maximum efficiency is 5.9%, 6.1%, and 6.4% for $\alpha_2 = 90°$, 60°, and 30°, respectively. Moreover, the maximum efficiency of the ECF micro-pump exists at a larger flow rate when α_2 decreases. This resembles the results shown in Fig. 7(a). This is because the decrease in downstream angle reduces the vortex formation downstream of the micro-pump, reducing the hydraulic losses. Hence, the ECF micro-pump efficiency generally increases. Fig. 7(b) presents the influence of α_2 on ECF micro-pumps' pressure difference (Δp). The applied voltage varies from 2 kV to 8 kV within 2 kV increments. It was found from this figure that Δp tends to decrease when α_2 increases, and the largest change occurs for the highest value of applied voltage. The decrease in Δp with increasing α_2 from 30° to 90° is 1.6%, 15.5%, 11.3%, and 9.8% for the four applied voltages of 2, 4, 6, and 8 kV, respectively, when comparing the Δp at $\alpha_2 = 30°$.

3.2. Effects of the collector electrode width

Fig. 8 shows the velocity and concentration distributions of the ECF flow under the effects of the collector width L_c. L_c varies from 0 to 4; the downstream angle, flow rate, and applied voltage are kept constant at specific values of 30°, 50 ml/h, and 4 kV, respectively. It was found that when L_c increases, both velocity and concentration field distributions change, particularly when L_c varies from 0 to 1. Then, the high-velocity region expands as the collector width increases, even though the maximum velocity decreases slightly from 56.62 to 56.39 when L_c ranges from 1 to 4. For the concentration field, the maximum concentration increases with L_c ranging from 0 to 1; however, it decreases with a further increase of L_c (from 13443 down to 10532), as shown in Fig. 8(b). This result predicts the optimum value of L_c at which the electro-hydraulic performance reaches a maximum.

Fig. 9 describes the variation of the streamline distribution of the ECF flow in the micro-pump for the four particular values of L_c that correspond to those in Fig. 8 for comparison purposes. It was found that at $L_c = 0$ (upper left figure), the vortex generated from the upstream to the downstream of the ECF micro-pump near the collector slit. This may cause higher hydrodynamic losses; hence, the efficiency is expected to be lower than in other operating cases. As L_c increases (greater than unity), the vortex areas form

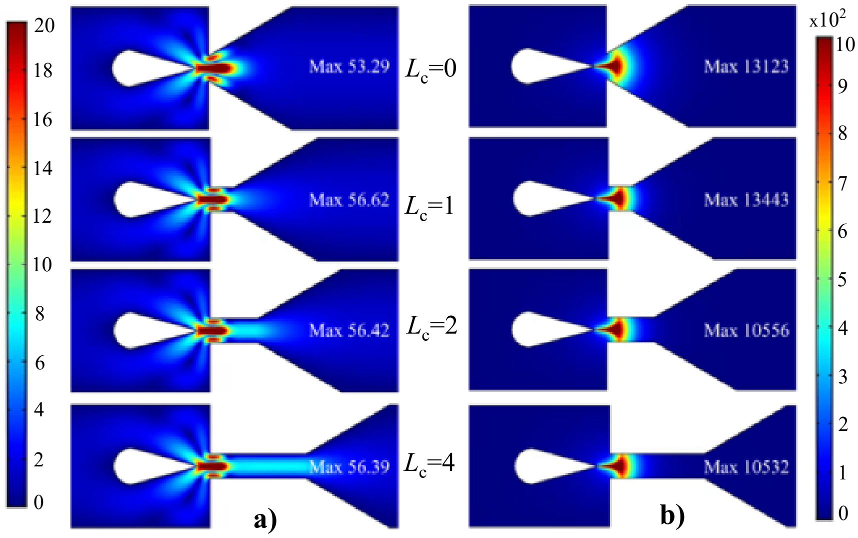

Fig. 8. (a) Velocity field and (b) concentration distributions for various values of L_c with $Q = 50$ ml/h and $\phi_0 = 4$ kV

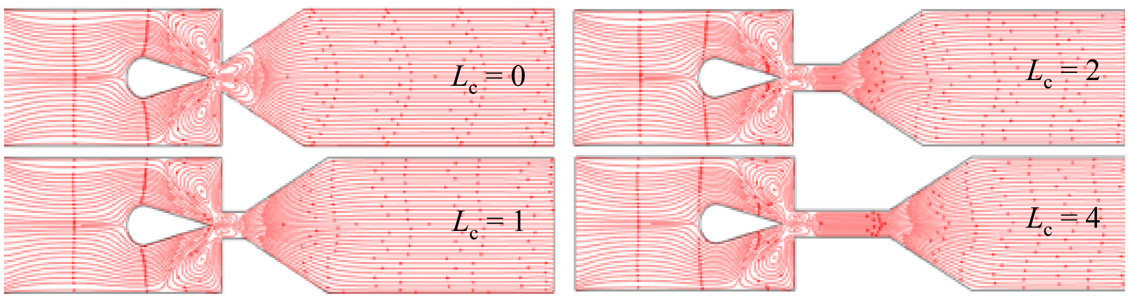

Fig. 9. Variation of streamline distributions for various values of L_c with $Q = 50$ ml/h and $\phi_0 = 4$ kV

only at the upstream and the entrance of the collector slit. However, if L_c is too large, the friction and hydraulic losses due to the large slit may increase, resulting in the reduction of the micro-pump efficiency. Therefore, again, it predicted that L_c has an optimal value at which the ECF micro-pumps obtained the highest efficiency due to the reduction of vortex formation and other losses. The influence of L_c on the performance of the ECF micro-pump can be explained as follows: For small L_c, the surface area of the collector electrode decreases, the charges emitted from the positive electrode tend to move back after passing through the short slit, resulting in the larger vortex region (Fig. 9, $L_c = 0$), then the flow resistance increases or the hydraulic power decreases, hence the pump efficiency reduces. On the other hand, for very large L_c, all the charges can be collected at the negative electrode because the collector's surface area is very large. The electric power slightly improves. However, the hydrodynamic losses increase overwhelmingly when the ECF flow moves in a small channel with high kinetic energy. Hence, the efficiency is also reduced in this case. This means that the optimal value of L_c exists to maximize the efficiency of an ECF micro-pump.

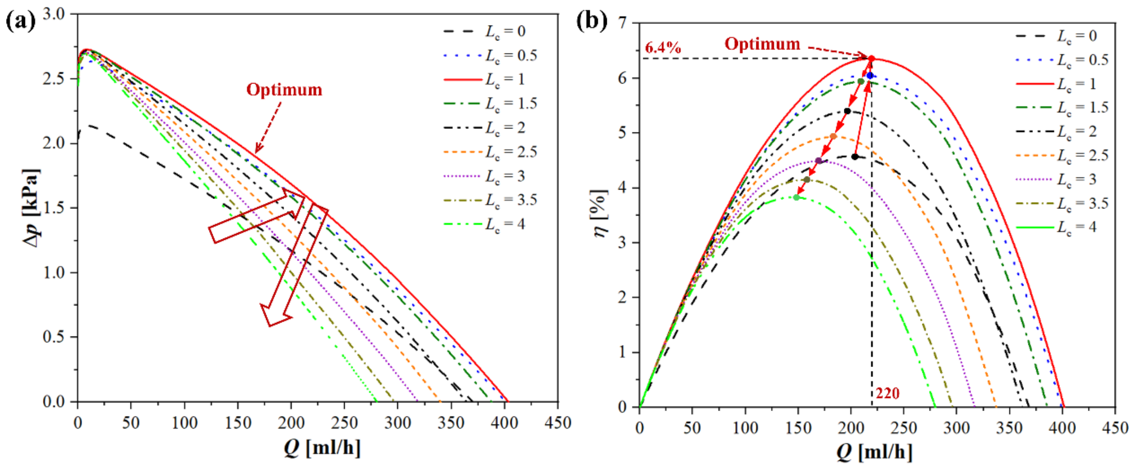

Fig. 10. (a) Δp–Q and (b) η–Q characteristic curves for various values of L_c with $\phi_0 = 4$ kV and $\alpha_2 = 30^\circ$

Fig. 10 shows the characteristic curves of the ECF micro-pump for various values of L_c with $\phi_0 = 4$ kV and $\alpha_2 = 30^\circ$. In this study, L_c ranges from 0 to 4 with a step change of 0.5. The results in Fig. 10(a) indicate that the operating range of the ECF micro-pump is generally extended with increasing L_c. The Δp and the flow rate of the ECF micro-pump tend to increase extensively. Particularly, the operating range of the ECF micro-pump becomes largest at $L_c = 1$ (the red solid curve in Fig. 10(a)). However, when L_c continued to increase from $L_c = 1$, the operating range of the pump gradually narrowed, which can be explained by the increase in friction and hydraulic losses when the ECF flow moved in the collector slit. Fig. 10(b) also indicates a significant impact of L_c on the performance curve of the ECF micro-pump. Connecting the extreme efficiency points (red arrows) to show the variation of the micro-pump efficiency with the change of L_c. The ECF micro-pump's performance curve peaked at $L_c = 1$, as represented by the red solid curve in Fig. 10(b), at which the maximum efficiency obtained was 6.4% and a flow rate of 220 ml/h.

Fig. 11 shows the variation of Δp and $\eta_{\max}$ as a function of L_c. α_2 was kept constant at 30° for all computational cases. The applied voltages ϕ_0 range from 2 to 8 kV. It was found from Fig. 11(a) that Δp increases with increasing L_c, then it reaches a maximum value at a specific L_c, and it decreases further. This trend is valid for all applied voltages considered. The maximum Δp values obtained were 0.34, 1.6, 3.7, and 7.8 kPa for ϕ_0 of 2,

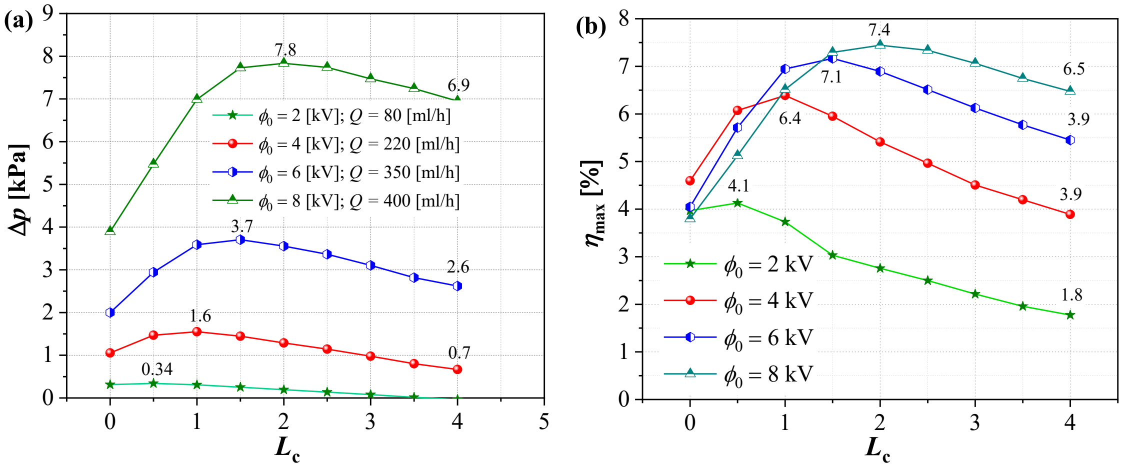

Fig. 11. Variation of (a) Δp and (b) $\eta_{\max}$ as a function of L_c for various values of ϕ_0, $\alpha_2 = 30^\circ$ was used for all cases

4, 6, and 8 kV, respectively. All extreme points from Fig. 10(b), but for many other values of applied voltages, are summarized in Fig. 11(b). The results indicate that, for a given applied voltage ϕ_0, $\eta_{\max}$ depends significantly on L_c. More clearly, the maximum efficiencies achieved were 4.1%, 6.4%, 7.1%, and 7.4% for L_c of 0.5, 1, 1.5, and 2, respectively. The maximum efficiency decreased with further increasing L_c, with the greatest reduction in maximum efficiency observed at $L_c = 4$. Furthermore, the results in Fig. 11(b) indicate that higher applied voltages on the electrodes lead to higher achievable efficiencies. Based on an extensive study, the L_c ranging from 0.5 to 2.0 is the optimum range for maximal efficiency. It means the collector width and its slit gap should be designed in this range to obtain the optimum operating point of this ECF micro-pump. The maximum efficiency obtained for the ECF micro-pump was 7.4% at $\phi_0 = 8$ kV and $L_c = 2.0$. This value is higher than any maximum efficiencies reported in previous studies, such as 3.2% by Ueno et al. [10] and 5% by Yanada et al. [24]. This point indicates the performance improvement in this ECF micro-pump design.

Although the micro-pump efficiency generally increases with increasing applied voltage (Figs. 7(b) and 11(b)), applying a high voltage may cause other problems. For example, it causes an increase in the micro-pump temperature, a decrease in electrode durability, and unfortunately, electrodes can be disrupted at sufficiently high values. Therefore, the applied voltage is less than a threshold value, e.g., less than 10 kV.

4. CONCLUSIONS

This study investigated the influence of the downstream angle α_2 and electrode width L_c on the fluid flow behavior in an ECF micro-pump. The finite element method was used to solve the multiphysics problem of ECF flow. Consequently, the results obtained from the present study can be drawn as follows:

- By increasing the electrode width L_c, the operating range of the ECF micro-pump can be extended. There is an optimal L_c value at which the efficiency of the micro-pump is maximized. The optimum range of L_c is from 0.5 to 2.0.

- Additionally, the operating range of the ECF micro-pump can be further extended by reducing the downstream angle α_2, especially at higher flow rates. Moreover, α_2 significantly impacts the formation of vortices within the ECF micro-pump, leading to an increase in hydraulic losses or a reduction in efficiency.

- The maximum efficiency of the ECF micro-pump was up to 7.4% at $\phi_0 = 8$ kV and $L_c = 2.0$.

DECLARATION OF COMPETING INTEREST

The authors declare that they have no known competing financial interests or personal relationships that could have appeared to influence the work reported in this paper.

ACKNOWLEDGMENT

This research is funded by Vietnam National Foundation for Science and Technology Development (NAFOSTED) under grant number 107.03-2021.37.

REFERENCES

[1] R.-J. Yang, H.-H. Hou, Y.-N. Wang, and L.-M. Fu. Micro-magnetofluidics in microfluidic systems: A review. *Sensors and Actuators B: Chemical*, **224**, (2016), pp. 1–15. https://doi.org/10.1016/j.snb.2015.10.053.

[2] Z. Mao, T. Nagaoka, S. Yokota, and J.-W. Kim. Soft fiber-reinforced bending finger with three chambers actuated by ECF (electro-conjugate fluid) pumps. *Sensors and Actuators A: Physical*, **310**, (2020). https://doi.org/10.1016/j.sna.2020.112034.

[3] S. Mohith, P. N. Karanth, and S. M. Kulkarni. Recent trends in mechanical micropumps and their applications: A review. *Mechatronics*, **60**, (2019), pp. 34–55. https://doi.org/10.1016/j.mechatronics.2019.04.009.

[4] Y.-N. Wang and L.-M. Fu. Micropumps and biomedical applications – a review. *Microelectronic Engineering*, **195**, (2018), pp. 121–138. https://doi.org/10.1016/j.mee.2018.04.008.

[5] K. Edamura, Y. Ohashi, and S. Yokota. *The use of electro-sensitive movable fluids, methods of using the same and motors for the electro-sensitive movable fluids*, (2002). European Patent.

[6] K. Mori, H. Yamamoto, K. Takemura, S. Yokota, and K. Edamura. Dominant factors inducing electro-conjugate fluid flow. *Sensors and Actuators A: Physical*, **167**, (1), (2011), pp. 84–90. https://doi.org/10.1016/j.sna.2011.01.009.

[7] V. Cacucciolo, J. Shintake, Y. Kuwajima, S. Maeda, D. Floreano, and H. Shea. Stretchable pumps for soft machines. *Nature*, **572**, (7770), (2019), pp. 516–519. https://doi.org/10.1038/s41586-019-1479-6.

[8] H. Sun, J. Zhao, Y. Zhang, and M. Xu. Flexible pump for small-scale soft robotics: actuation, design and prospects. *Measurement*, **237**, (2024). https://doi.org/10.1016/j.measurement.2024.115299.

[9] T. Matsubara, H. H. Huynh, K. Yoshida, and J.-W. Kim. Development of MEMS-fabricated bidirectional ECF (electro-conjugate fluid) micropumps. *Sensors and Actuators A: Physical*, **295**, (2019), pp. 317–323. https://doi.org/10.1016/j.sna.2019.06.022.

[10] S. Ueno, K. Takemura, S. Yokota, and K. Edamura. Micro inchworm robot using electro-conjugate fluid. *Sensors and Actuators A: Physical*, **216**, (2014), pp. 36–42. https://doi.org/10.1016/j.sna.2014.04.032.

[11] J.-W. Kim, T. Suzuki, S. Yokota, and K. Edamura. Tube-type micropump by using electro-conjugated fluid (ECF). *Sensors and Actuators A: Physical*, **174**, (2012), pp. 155–161. https://doi.org/10.1016/j.sna.2011.10.027.

[12] J.-W. Kim, Y. Yamada, and S. Yokota. Micro ECF (electro-conjugate fluid) hydraulic power sources based on the modular design of TPSEs (triangular prism and slit electrode pairs). *The International Journal of Advanced Manufacturing Technology*, **106**, (1-2), (2020), pp. 627–639. https://doi.org/10.1007/s00170-019-04598-x.

[13] S. Yokota, K. Kawamura, K. Takemura, and K. Edamura. High-integration micromotor using electro-conjugate fluid (ECF). *Journal of Robotics and Mechatronics*, **17**, (2), (2005), pp. 142–148. https://doi.org/10.20965/jrm.2005.p0142.

[14] T. Otomo, T. Matsubara, K. Yoshida, D.-H. Kim, M. Ikeuchi, and J.-W. Kim. A microfluidic device integrated with a stretchable microporous membrane controlled by electro-conjugate fluid. *Sensors and Actuators A: Physical*, **356**, (2023). https://doi.org/10.1016/j.sna.2023.114332.

[15] Y. Kuroboshi, K. Takemura, and K. Edamura. Efficient electrode configuration for electro-conjugate fluid flow generation with dibutyl decanedioate: Experimental and theoretical investigation. *Sensors and Actuators A: Physical*, **279**, (2018), pp. 223–228. https://doi.org/10.1016/j.sna.2018.06.018.

[16] W.-S. Seo, K. Yoshida, S. Yokota, and K. Edamura. A high performance planar pump using electro-conjugate fluid with improved electrode patterns. *Sensors and Actuators A: Physical*, **134**, (2), (2007), pp. 606–614. https://doi.org/10.1016/j.sna.2006.06.027.

[17] R. V. Raghavan, J. Qu, L. Y. Yeo, J. R. Friend, K. Takemura, S. Yokota, and K. Edamura. Electrokinetic actuation of low conductivity dielectric liquids. *Sensors and Actuators B: Chemical*, **140**, (1), (2009), pp. 287–294. https://doi.org/10.1016/j.snb.2009.04.020.

[18] D. Han, H. Wang, S. Yokota, and J.-W. Kim. Configurations of triangular prism and slit electrode pairs to enhance the performance of electro-conjugate fluid micropumps. *Journal of Micromechanics and Microengineering*, **30**, (2), (2020). https://doi.org/10.1088/1361-6439/ab5ef3.

[19] T. K. Lai, T. Dinh, M. D. Nguyen, and I. L. Ngo. A new design of electro-conjugate fluid micropumps with Venturi and teardrop-shaped electrodes. *Physics of Fluids*, **36**, (9), (2024). https://doi.org/10.1063/5.0221203.

[20] H. C. Chang and L. Y. Yeo. *Electrokinetically driven microfluidics and nanofluidics*. Cambridge University Press, New York, (2010).

[21] W. K. H. Panofsky and M. Phillips. *Classical Electricity and Magnetism*. Addison-Wesley Publishing Company, Cambridge, MA, (1961).

[22] K. D. Tran, Y. Kikuchi, and H. Yanada. Measurement and numerical simulation of flow and electric fields in charge injection type of electrostatic oil filter. *Transactions of the Japan Fluid Power System Society*, **40**, (1), (2009), pp. 8–15. https://doi.org/10.5739/jfps.40.8.

[23] M. Nishikawara, M. Shimada, M. Saigo, and H. Yanada. Numerical investigation of the characteristics of an ion drag pump. *Journal of Electrostatics*, **84**, (2016), pp. 23–31. https://doi.org/10.1016/j.elstat.2016.08.001.

[24] H. Yanada, S. Hakama, T. Miyashita, and N. Zhang. An investigation of an ion drag pump using a needle-mesh electrode configuration. *Proceedings of the Institution of Mechanical Engineers, Part C: Journal of Mechanical Engineering Science*, **216**, (3), (2002), pp. 325–334. https://doi.org/10.1243/0954406021525034.